



The energetics of pilot-wave hydrodynamics

Matthew Durey¹ and John W.M. Bush²

¹School of Mathematics and Statistics, University of Glasgow, University Place, Glasgow G12 8QQ, UK

²Department of Mathematics, Massachusetts Institute of Technology, Cambridge, MA 02139, USA

Corresponding author: Matthew Durey, matthew.durey@glasgow.ac.uk

(Received 16 July 2024; revised 18 December 2024; accepted 4 February 2025)

A millimetric droplet may bounce and self-propel across the surface of a vertically vibrating liquid bath, guided by the slope of its accompanying Faraday wave field. The ‘walker’, consisting of a droplet dressed in a quasi-monochromatic wave form, is a spatially extended object that exhibits many phenomena previously thought exclusive to the quantum realm. While the walker dynamics can be remarkably complex, steady and periodic states arise in which the energy added by the bath vibration necessarily balances that dissipated by viscous effects. The system energetics may then be characterised in terms of the exchange between the bouncing droplet and its guiding or ‘pilot’ wave. We here characterise this energy exchange by means of a theoretical investigation into the dynamics of the pilot-wave system when time-averaged over one bouncing period. Specifically, we derive simple formulae characterising the dependence of the droplet’s gravitational potential energy and wave energy on the droplet speed. Doing so makes clear the partitioning between the gravitational, wave and kinetic energies of walking droplets in a number of steady, periodic and statistically steady dynamical states. We demonstrate that this partitioning depends exclusively on the ratio of the droplet speed to its speed limit.

Key words: drops, Faraday waves

1. Introduction

The hydrodynamic pilot-wave system (Bush 2010), discovered in 2005 by Yves Couder and Emmanuel Fort (Couder *et al.* 2005*a*) has garnered considerable interest owing to its relation to quantum systems (Couder *et al.* 2005*b*), and has provided the basis for the field of hydrodynamic quantum analogues (Bush & Oza 2021). The system consists of a millimetric droplet bouncing on the surface of a vibrating liquid bath. The vibrational acceleration is always less than the Faraday threshold (Benjamin & Ursell 1954; Kumar &

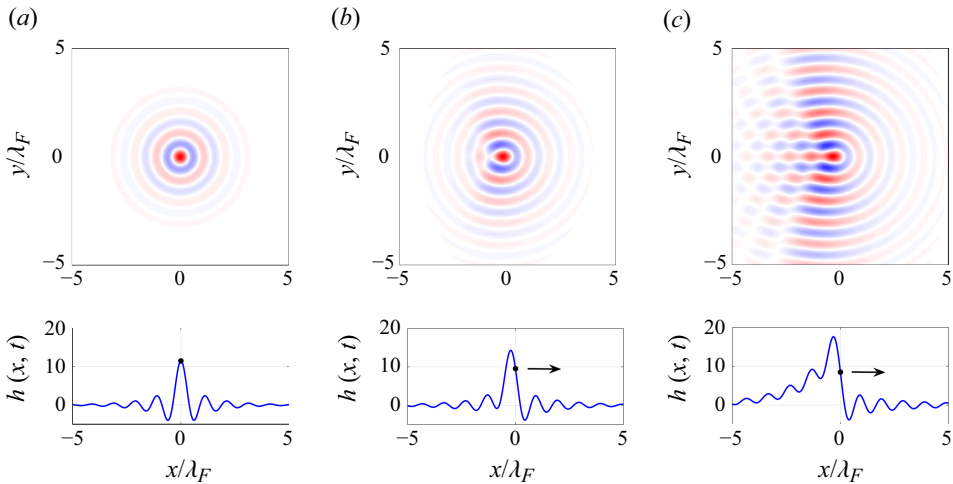


Figure 1. Stroboscopic pilot-wave fields, $h(x, t)$, generated by (a) a stationary bouncer and (b, c) walkers for vibrational forcing (a) $\gamma = \gamma_W$ (the walking threshold), (b) $\gamma/\gamma_F = 0.9$ and (c) $\gamma/\gamma_F = 0.97$. Upper panels: overhead view of the stroboscopic wave field accompanying the droplet, with regions of elevation and depression highlighted in red and blue, respectively. Lower panels: the wave profile (in μm) along the line of droplet motion. The droplet speed and wave energy increase with the vibrational forcing, with the wave field spanning the plane in the high-memory limit. As the droplet moves faster, it moves away from the wave crest towards a region with higher slope, inducing a corresponding decrease in the local wave elevation. The plots are generated by solving the stroboscopic pilot-wave model (2.1) for walking at a constant speed (see (4.3)) with physical parameters $f = 80$ Hz, $\rho = 950$ kg m $^{-3}$, $\nu = 20.9$ cSt, $\sigma = 0.206$ N m $^{-1}$, $\mathcal{H} = 4$ mm, $R = 0.4$ mm, $\sin \Phi = 0.2$, and $T_d = 0.0174$ s (see table 1). The walking threshold is $\gamma_W/\gamma_F = 0.782$, the Faraday wavelength is $\lambda_F = 4.75$ mm and the maximum steady walking speed is $c = 13.3$ mm s $^{-1}$.

Tuckerman 1994; Kumar 1996), above which Faraday waves arise even in the absence of the droplet, so the wave field navigated by the droplet is always entirely of its own making. The control parameter of the system is the bath’s vibrational acceleration, which prescribes the longevity of the waves generated by the droplet impacts, and so the ‘memory’ of the system (Eddi *et al.* 2011). Increasing the memory progressively towards the Faraday threshold prompts the stationary bouncing droplet to destabilise into a ‘walker’, a macroscopic realisation of wave–particle duality consisting of a self-propelling droplet dressed in a quasi-monochromatic pilot-wave form (Bush 2015; Bush & Oza 2021). As the memory is further increased, the walking speed and spatial extent of the wave field increase, while the droplet moves downwards on its pilot wave, towards a region with higher slope (see figure 1).

The hydrodynamic pilot-wave system is driven and dissipative (Kutz *et al.* 2022; Rahman & Kutz 2023); specifically, energy is fed into the system through the bath vibration and dissipated through the action of fluid viscosity. This dissipation ultimately leads to a warming of the bath and an associated drift of the Faraday threshold (Douady 1990; Harris *et al.* 2013; Ellegaard & Levinsen 2020). Nevertheless, a number of steady, periodic and statistically steady dynamical states may be achieved in which the driving and dissipation effectively balance over the time scales of interest (seconds or minutes), so that the global energetics need not be considered. Examples include steady walking states and orbital motion when the droplet moves in response to an external force field (Fort *et al.* 2010; Harris & Bush 2014; Perrard *et al.* 2014b). The existence and stability of the system’s various dynamical states change with the vibrational forcing, which in turn prescribes the spatial extent and longevity of the wave field. In the high-memory

limit, the pilot-wave dynamics often appears chaotic (Tambasco *et al.* 2016), with the droplet motion intermittently switching between weakly unstable periodic states (Harris & Bush 2014; Perrard *et al.* 2014a). A number of connections have been made between the energy of different dynamical states and their relative stability. For example, stable steady walking, orbiting and periodic states are all energetically favourable relative to unstable stationary bouncing (Durey & Milewski 2017; Durey *et al.* 2018; Liu *et al.* 2023). Energetic considerations also arise in bound states formed from multiple droplets. For example, the wave energy of promenading pairs (Arbelaiz *et al.* 2018), consisting of two coupled droplets walking in tandem, is less than that of two free walkers (Borghesi *et al.* 2014; Durey & Milewski 2017). Finally, rings of bouncing droplets destabilise and execute a number of discrete rearrangements in such a way as to minimise their net gravitational potential energy (Couchman & Bush 2020; Thomson *et al.* 2020b).

Despite the growing number of connections between energy and stability, a global account of the energy evolution of the pilot-wave system has not been forthcoming. One recent advancement, however, was made by Liu *et al.* (2023), who demonstrated that for droplets executing circular orbits, the wave energy and the droplet gravitational potential energies are both prescribed by the droplet speed. Through systematic analysis of the system energetics, we here demonstrate the generality of this result by deriving a speed-dependent energy diminution factor relating the wave energy and drop gravitational potential energy of dynamic states to those of the static bouncing state. Our results are valid for a number of canonical settings, including steady and quasi-steady dynamics, periodic and slow oscillatory dynamics and statistically steady states.

In § 2, we introduce the pilot-wave system and determine evolution equations for the wave and droplet energies. We utilise these results in § 3 to determine the dependence of energy on the droplet's speed for canonical dynamical and statistically steady states. A number of illustrative numerical examples are presented in § 4. In § 5, we enumerate insights into pilot-wave hydrodynamics provided by our energetic analysis.

2. Pilot-wave hydrodynamics

We consider a vertically vibrating liquid with periodic acceleration $\gamma \sin(2\pi ft)$ at time t . All relevant parameters are defined in table 1. For $\gamma > \gamma_F$, the fluid rest state destabilises to a field of subharmonic standing or Faraday waves, with wavelength $\lambda_F = 2\pi/k_F$ and period $T_F = 2/f$. Below the Faraday threshold, $\gamma < \gamma_F$, any waves generated at the free surface, for example by a bouncing droplet, are subcritical, decaying over a time scale, T_M , that increases with proximity to the Faraday threshold. For the weakly viscous liquids used in experiments (Wind-Willassen *et al.* 2013), the Faraday wavenumber, k_F , approximately satisfies the gravity–capillary dispersion relation, $(\pi f)^2 = (gk_F + \sigma k_F^3/\rho) \tanh(k_F \mathcal{H})$ (Benjamin & Ursell 1954).

2.1. Governing equations

We model the evolution of a resonant walker bouncing with period T_F , in perfect synchrony with its subharmonic pilot wave, $\eta(\mathbf{x}, t)$. We thus assume that each drop impact arises at the same wave amplitude and phase, the basis of the stroboscopic approximation (Oza *et al.* 2013). The droplet is propelled by the wave force $\mathbf{F}_w(t) = -F(t)\nabla\eta(\mathbf{x}_p, t)$ and resisted by drag, where $\mathbf{x}_p(t)$ denotes the droplet's horizontal position at time t and $F(t)$ is the periodic vertical force acting on the droplet. Notably, the vertical force averaged over one bouncing period, T_F , is precisely equal to the droplet weight, namely $\overline{F(t)} = mg$. As the time scale of the droplet's horizontal motion greatly exceeds that of its vertical motion, we model the wave field as $\eta(\mathbf{x}, t) = \cos(\pi ft)\bar{\eta}(\mathbf{x}, t)$, representing the superposition of

Parameter	Definition
m, R	Droplet mass, radius
σ, ρ	Liquid surface tension, density
ν, ν_{eff}	(Effective) liquid kinematic viscosity
\mathcal{H}, g	Liquid bath depth, gravitational acceleration
$\mu_{\text{air}}, \rho_{\text{air}}$	Air dynamic viscosity, density
f, γ	Vibrational forcing frequency, acceleration
γ_F	Faraday instability threshold
$\lambda_F, k_F = 2\pi/\lambda_F, T_F = 2/f$	Faraday wavelength, wavenumber, period
$T_d = (\nu_{\text{eff}}k_F^2)^{-1}$	Wave decay time in the absence of forcing
$T_M = T_d/(1 - \gamma/\gamma_F)$	Wave decay time
$F(t)$	Periodic vertical force acting on the droplet
$\overline{F(t)} = mg$	Vertical force averaged over Faraday period
$\mathcal{S} = \overline{F(t) \sin(\pi f t)}/mg$	Phase of droplet impact for wave generation
$\mathcal{C} = \overline{F(t) \cos(\pi f t)}/mg$	Phase of droplet impact relative to wave oscillation
$\sin \Phi = 2\mathcal{S}\mathcal{C}$	Combined phase parameter
$A = \sqrt{\nu_{\text{eff}}T_F/2\pi(mgk_F^3 \sin \Phi)/(3k_F^2\sigma + \rho g)}$	Amplitude of single surface wave
$D = 0.17mg\sqrt{\rho R/\sigma} + 6\pi\mu_{\text{air}}R(1 + (\rho_{\text{air}}gR/12\mu_{\text{air}}f))$	Drag coefficient
$c = \sqrt{mgA/DT_F}$	Maximum steady walking speed
$H_B = AT_M/T_F$	Amplitude of stroboscopic bouncer wave field
$\mathcal{H}(r)$	Wave kernel spatial profile
$l_d(\gamma)$	Wave kernel spatial decay length
$\alpha = \epsilon^2/[2\nu_{\text{eff}}(1 + 2\epsilon^2)]$	Spatial damping factor
$\epsilon = 2\pi f\rho\nu_{\text{eff}}k_F/[3\sigma k_F^2 + \rho g]$	Viscosity-induced wavenumber correction
$\eta(\mathbf{x}, t), \mathcal{E}(t)$	Faraday wave field, energy
$h(\mathbf{x}, t), E(t)$	Stroboscopic wave field, energy
$\overline{\mathcal{E}} = (1/2)E/\mathcal{C}^2$	Faraday wave energy averaged over Faraday period
E_p	Stroboscopic droplet energy
$\mathcal{E} = E_p + E$	Total stroboscopic energy

Table 1. Table of parameters defining the stroboscopic pilot-wave model (Moláček & Bush 2013a,b; Oza *et al.* 2013).

a fast subharmonic oscillation modulated by a slowly varying spatial profile (Moláček & Bush 2013b). Time-averaging the droplet wave force over one bouncing period thus yields $\overline{\mathbf{F}_w(t)} = -mg\nabla h(\mathbf{x}_p, t)$, where $h(\mathbf{x}, t) = \mathcal{C}\overline{\eta}(\mathbf{x}, t)$ is the stroboscopic wave field and $\mathcal{C} = \overline{F(t) \cos(\pi f t)}/mg$ denotes the phase of droplet impact relative to the wave-field oscillation (Moláček & Bush 2013b; Couchman *et al.* 2019). The time-averaged horizontal force balance may then be written as (Moláček & Bush 2013b)

$$m\ddot{\mathbf{x}}_p + D\dot{\mathbf{x}}_p = -mg\nabla h(\mathbf{x}_p, t) + \mathbf{F}, \quad (2.1a)$$

where \mathbf{F} is an applied force and dots denote derivatives with respect to time.

We model the stroboscopic pilot wave by the integral

$$h(\mathbf{x}, t) = \frac{A}{T_F} \int_{-\infty}^t \mathcal{H}(|\mathbf{x} - \mathbf{x}_p(s)|) e^{-(t-s)/T_M} ds, \quad (2.1b)$$

which represents a superposition of axisymmetric quasi-monochromatic waves of amplitude A centred along the droplet's path and decaying over the memory time scale, T_M (Oza *et al.* 2013). Experimentally, this represents the wave form observed when the system is strobed at the Faraday frequency, and images captured at the phase of droplet

impact, so that the droplet appears to surf along its pilot wave. The system (2.1) represents the stroboscopic model (Oza *et al.* 2013) of pilot-wave hydrodynamics, which has proven to be adequate in rationalising the bulk of observed walker behaviours (Oza *et al.* 2014a; Turton *et al.* 2018). Nevertheless, it is known to have shortcomings when non-resonant effects arise (Primkulov *et al.* 2025), specifically when the walker bouncing phase varies owing to variability in the local wave form (Harris *et al.* 2013; Durey *et al.* 2020), which is particularly prevalent at high memory (Moláček & Bush 2013b; Wind-Willassen *et al.* 2013). Consequently, the results of our study are unlikely to be applicable in experiments close to the Faraday threshold, for which exotic and chaotic bouncing modes (Protière *et al.* 2006; Wind-Willassen *et al.* 2013) are expected to significantly alter the pilot-wave energetics.

For the sake of simplicity, we proceed by focusing on the case of resonant walkers, and so neglect temporal variations in the droplet impact phase. We may thus treat the wave amplitude, A , as a constant. We further assume that the wave kernel, $\mathcal{H}(r)$, is a differentiable function, with $\mathcal{H}(0) = 1$ and $\mathcal{H}(r) < 1$ for all $r > 0$. Furthermore, we posit that the spectrum is localised about k_F , giving rise to a quasi-monochromatic form with wavelength λ_F and exponential spatial decay in the farfield over the length scale l_d . Motivated by the results of prior studies (Tadrist *et al.* 2018; Couchman *et al.* 2019), we assume that $l_d(\gamma)$ increases with the vibrational forcing, and diverges in the high-memory limit.

2.2. Droplet energy evolution

We proceed by describing the evolution of the droplet’s kinetic and potential energy, where we express our results in terms of the local wave height, $H(t) = h(\mathbf{x}_p, t)$. We first use the chain rule to write $\dot{H} = \partial_t h(\mathbf{x}_p, t) + \dot{\mathbf{x}}_p \cdot \nabla h(\mathbf{x}_p, t)$, whereupon substitution of (2.1) yields

$$\dot{H} = \frac{A}{T_F} - \frac{H}{T_M} + \frac{1}{mg} \dot{\mathbf{x}}_p \cdot (\mathbf{F} - m\ddot{\mathbf{x}}_p - D\dot{\mathbf{x}}_p). \quad (2.2)$$

We then rearrange to find that the droplet’s energy evolves according to

$$\frac{d}{dt} \left(\frac{1}{2} m |\dot{\mathbf{x}}_p|^2 + mgH \right) = \dot{\mathbf{x}}_p \cdot \mathbf{F} + \frac{mgA}{T_F} \left(\gamma_D(|\dot{\mathbf{x}}_p|) - \frac{H}{H_B} \right), \quad (2.3)$$

where $H_B = AT_M/T_F$ is the amplitude of the stroboscopic wave field for a bouncer,

$$\gamma_D(v) = 1 - \frac{v^2}{c^2} \quad (2.4)$$

is a speed-dependent diminution factor and $c = \sqrt{mgA/DT_F}$ is the maximum steady walking speed of a free walker, as arises in the high-memory limit (Oza *et al.* 2013).

For a droplet moving in response to the gradient of an applied potential, $\mathbf{F} = -\nabla V(\mathbf{x}_p)$, we may recast (2.3) as the work equation, as prescribes the rate of change of the droplet’s total energy:

$$\dot{E}_p = \frac{mgA}{T_F} \left(\gamma_D(|\dot{\mathbf{x}}_p|) - \frac{H}{H_B} \right), \quad \text{where} \quad E_p = \frac{1}{2} m |\dot{\mathbf{x}}_p|^2 + V(\mathbf{x}_p) + mgH \quad (2.5)$$

is the sum of the droplet’s dimensionless kinetic and potential energies. Evidently, the droplet energy increases when $H/H_B < \gamma_D(|\dot{\mathbf{x}}_p|)$, remains constant when $H/H_B = \gamma_D(|\dot{\mathbf{x}}_p|)$ and decreases otherwise. The implications of (2.5) for the system’s energy budget are discussed in [Appendix A](#).

2.3. Wave-field energy evolution

For near-critical vibrational forcing, the evolution of the Faraday wave field, $\eta(\mathbf{x}, t)$, may be regarded as quasi-inviscid, characterised by an exchange between kinetic energy and a combination of gravitational potential and surface energies. We thus define the gravitational potential and surface energies for small-amplitude waves (i.e. $|\nabla\eta| \ll 1$) as (Moláček & Bush 2013b)

$$\mathcal{E}(t) = \iint_{\mathbb{R}^2} \frac{\rho g}{2} \eta^2(\mathbf{x}, t) \, d\mathbf{x} + \iint_{\mathbb{R}^2} \frac{\sigma}{2} |\nabla\eta|^2 \, d\mathbf{x}. \tag{2.6}$$

Owing to the assumed far-field exponential decay of the wave field, the integrals in (2.6) converge, which is not the case for the widely adopted and mathematically convenient choice $\mathcal{H}(r) = J_0(k_F r)$ (Liu *et al.* 2023), an account of which is given in Appendix B.

By substituting the relationship $\eta(\mathbf{x}, t) = \cos(\pi f t) h(\mathbf{x}, t) / \mathcal{C}$ into (2.6), we deduce that the energy of the wave field when time-averaged over one Faraday period, denoted $\overline{\mathcal{E}(t)}$, is related to the energy of the stroboscopic pilot wave,

$$E(t) = \iint_{\mathbb{R}^2} \frac{\rho g}{2} h^2(\mathbf{x}, t) \, d\mathbf{x} + \iint_{\mathbb{R}^2} \frac{\sigma}{2} |\nabla h|^2 \, d\mathbf{x}, \tag{2.7}$$

via $\overline{\mathcal{E}} = \frac{1}{2} E / \mathcal{C}^2$. As \mathcal{C} typically lies in the range $0.1 \lesssim \mathcal{C} \lesssim 0.2$ for walkers (Couchman *et al.* 2019), the time-averaged wave-field energy is at least one order of magnitude larger than the energy of the stroboscopic pilot wave. Nevertheless, we leverage this proportionality relationship to derive a simple formula governing the evolution for E , and thus $\overline{\mathcal{E}}$.

To proceed, we recast the stroboscopic pilot wave as

$$h(\mathbf{x}, t) = \sum_{n=-\infty}^{\infty} \int_0^{\infty} k \hat{h}_n(k, t) \Phi_n(\mathbf{x}, k) \, dk, \tag{2.8a}$$

where $\Phi_n(\mathbf{x}, k) = J_n(kr) e^{in\theta}$ denotes an orthogonal set of functions defined in plane polar coordinates, $\mathbf{x} = r(\cos \theta, \sin \theta)$, J_n is the Bessel function of the first kind of order n , k is the wavenumber and i denotes the imaginary unit. In terms of this basis decomposition, the stroboscopic wave energy defined in (2.7) is (Moláček & Bush 2013b)

$$E(t) = \pi \sum_{n=-\infty}^{\infty} \int_0^{\infty} k(\rho g + \sigma k^2) |\hat{h}_n(k, t)|^2 \, dk. \tag{2.8b}$$

Furthermore, an application of Graf's addition theorem (Abramowitz & Stegun 1964, 9.1.79) to (2.1b) determines that each wave mode evolves according to

$$\hat{h}_n(k, t) = \frac{\hat{h}_B(k)}{T_M} \int_{-\infty}^t \Phi_n^*(\mathbf{x}_p(s), k) e^{-(t-s)/T_M} \, ds, \tag{2.9}$$

where $*$ denotes complex conjugation and $\hat{h}_B(k) = \int_0^{\infty} r h_B(r) J_0(kr) \, dr$ is the Hankel transform of the bouncer wave field, defined as $h_B(r) = H_B \mathcal{H}(r)$ with $H_B = AT_M / T_F$.

We now exploit the fact that the spectrum of the bouncer wave field is sharply peaked around k_F , with $\hat{h}_B(k)$ being appreciable only when $|k - k_F| l_d = O(1)$, to determine approximate expressions for $H(t)$ and $E(t)$ valid in the high-memory limit, for which $l_d k_F \gg 1$. To facilitate this analysis, we first substitute the leading-order Taylor expansion $\Phi_n^*(\mathbf{x}_p, k) = \Phi_n^*(\mathbf{x}_p, k_F) + O(\Delta k)$ (where $\Delta k = k/k_F - 1$) into (2.9), giving

$$\frac{\hat{h}_n(k, t)}{\hat{h}_B(k)} = \frac{1}{T_M} \int_{-\infty}^t \Phi_n^*(\mathbf{x}_p(s), k_F) e^{-(t-s)/T_M} ds + O(\Delta k) = \frac{\hat{h}_n(k_F, t)}{\hat{h}_B(k_F)} + O(\Delta k), \tag{2.10}$$

or, equivalently,

$$\frac{\hat{h}_n(k, t)}{\hat{h}_n(k_F, t)} = \frac{\hat{h}_B(k)}{\hat{h}_B(k_F)} + O(\Delta k). \tag{2.11}$$

This relationship demonstrates that the spectrum close to k_F is proportional to that of the bouncer wave field, which we exploit below to approximate the local wave height, $H(t)$, and stroboscopic wave energy, $E(t)$.

To approximate the local wave height, $H(t) = h(\mathbf{x}_p, t)$, we substitute $\Phi_n(\mathbf{x}_p, k) = \Phi_n(\mathbf{x}_p, k_F) + O(\Delta k)$ and (2.11) into (2.8a), and then exploit the fact that the integrand is sharply peaked about k_F for $l_d k_F \gg 1$, giving

$$H(t) = \sum_{n=-\infty}^{\infty} \frac{\hat{h}_n(k_F, t)}{\hat{h}_B(k_F)} \Phi_n(\mathbf{x}_p, k_F) \int_0^{\infty} k \hat{h}_B(k) dk + O((k_F l_d)^{-1}). \tag{2.12}$$

By noting that $h_B(0) = \int_0^{\infty} k \hat{h}_B(k) dk$, where $h_B(0) = H_B$ is the amplitude of the bouncer wave field, we deduce that

$$H(t) = H_B \sum_{n=-\infty}^{\infty} \frac{\hat{h}_n(k_F, t)}{\hat{h}_B(k_F)} \Phi_n(\mathbf{x}_p(t), k_F) + O((k_F l_d)^{-1}), \tag{2.13a}$$

thereby approximating the local wave height in terms of the system's wave modes. Likewise, we substitute (2.11) into (2.8b), giving

$$E(t) = \pi \sum_{n=-\infty}^{\infty} \frac{|\hat{h}_n(k_F, t)|^2}{\hat{h}_B^2(k_F)} \int_0^{\infty} k(\rho g + \sigma k^2) \hat{h}_B^2(k) dk + O((k_F l_d)^{-1}), \tag{2.13b}$$

where we have used that $\hat{h}_B(k)$ is real. This expression may be written more concisely as

$$E(t) = E_B \sum_{n=-\infty}^{\infty} \frac{|\hat{h}_n(k_F, t)|^2}{\hat{h}_B^2(k_F)} + O((k_F l_d)^{-1}), \tag{2.13c}$$

where

$$E_B = \pi \int_0^{\infty} k(\rho g + \sigma k^2) \hat{h}_B^2(k) dk \tag{2.14}$$

is the energy of the bouncer wave field. We thus deduce from (2.13) that H and E deviate from their respective values for a stationary bouncing droplet, denoted H_B and E_B , according to a weighted sum of the wave modes with wavenumber k_F . These approximations form the foundation for our forthcoming analysis of the energy evolution of the stroboscopic wave field.

To determine the evolution of $E(t)$, we first differentiate (2.9) and (2.13c) with respect to time. By neglecting higher-order connections of size $O((k_F l_d)^{-1})$ in the high-memory limit, corresponding to $k_F l_d \gg 1$, we deduce that

$$\frac{\partial \hat{h}_n}{\partial t} = \frac{\hat{h}_B(k)}{T_M} \Phi_n^*(\mathbf{x}_p(t), k) - \frac{\hat{h}_n}{T_M} \quad \text{and} \quad \frac{dE}{dt} = E_B \sum_{n=-\infty}^{\infty} \frac{2\text{Re}[\partial_t \hat{h}_n^*(k_F, t) \hat{h}_n(k_F, t)]}{\hat{h}_B^2(k_F)}, \tag{2.15}$$

respectively, where Re denotes the real part. By eliminating $\partial_t \hat{h}_n^*(k_F, t)$ from the second equation and using (2.13c), we obtain

$$\frac{T_M}{2} \frac{dE}{dt} = E_B \sum_{n=-\infty}^{\infty} \frac{\hat{h}_n(k_F, t)}{\hat{h}_B(k_F)} \Phi_n(\mathbf{x}_p(t), k_F) - E. \quad (2.16)$$

Finally, we use the approximate definition for $H(t)$ given in (2.13a) to deduce the leading-order evolution equation for the wave energy:

$$\frac{dE}{dt} = \frac{2E_B}{T_M} \left(\frac{H(t)}{H_B} - \frac{E(t)}{E_B} \right). \quad (2.17)$$

The wave energy increases when the ratio of the wave height relative to a bouncer exceeds the corresponding ratio for wave energy, and decreases otherwise. Equation (2.17) represents a powerful formula for elucidating the evolution of wave energy in pilot-wave hydrodynamics, the implications of which for the system's energy budget are discussed in Appendix A. We proceed by considering its application in a series of canonical dynamical regimes.

3. Energy evolution for canonical pilot-wave phenomena

Although the range of dynamics observed in experiments and predicted by the stroboscopic pilot-wave model (2.1) is vast (Bush 2015; Bush & Oza 2021), the qualitative behaviour may often be characterised by a small number of canonical regimes. To address the evolution of energy in these canonical regimes, we analyse the evolution formulae for the droplet and wave energy, as detailed in (2.5) and (2.17), respectively. Our results shed light on the dependence of energy on the droplet speed in a number of dynamical states.

The first canonical regime describes steady pilot-wave dynamics, for which the droplet and wave energies are conserved (Kutz *et al.* 2022; Liu *et al.* 2023; Rahman & Kutz 2023), as is the case for walking and orbiting at a constant speed. We thus deduce from (2.5) and (2.17) the respective relationships

$$H/H_B = \gamma_D(|\dot{\mathbf{x}}_p|) \quad \text{and} \quad E/E_B = H/H_B, \quad (3.1a)$$

giving rise to the following expressions for the droplet and wave energies:

$$E_p = \frac{1}{2} m |\dot{\mathbf{x}}_p|^2 + V(\mathbf{x}_p) + mgH_B \gamma_D(|\dot{\mathbf{x}}_p|) \quad \text{and} \quad E = E_B \gamma_D(|\dot{\mathbf{x}}_p|). \quad (3.1b)$$

Notably, the wave and droplet gravitational potential energies are both maximised for a stationary droplet, and decrease as the droplet walks faster and its kinetic energy increases. We thus deduce that the wave energy of a walker is always less than the wave energy of the unstable bouncer at the same vibrational forcing, providing a theoretical rationale for the observations made by Durey & Milewski (2017) based on their numerical computations.

The second canonical dynamical regime is periodic droplet motion, for which the average droplet and wave energies are conserved over one periodic cycle (Kutz *et al.* 2022; Rahman & Kutz 2023), as is the case for wobbling and drifting orbital states in a rotating frame (Harris & Bush 2014), and lemniscate and trefoil trajectories in a central force (Perrard *et al.* 2014b). In order to determine the average wave height, $\langle H \rangle$, and wave energy, $\langle E \rangle$, over one periodic cycle, we time-average (2.5) and (2.17), giving

$$\langle H \rangle / H_B = \gamma_D(\bar{v}) \quad \text{and} \quad \langle E \rangle / E_B = \langle H \rangle / H_B, \quad (3.2a)$$

where $\bar{v} = \sqrt{\langle |\dot{\mathbf{x}}_p|^2 \rangle}$ is the time-averaged droplet speed. Consequently,

$$\langle E_p \rangle = \frac{1}{2} m \bar{v}^2 + \langle V(\mathbf{x}_p) \rangle + mgH_B \gamma_D(\bar{v}) \quad \text{and} \quad \langle E \rangle = E_B \gamma_D(\bar{v}), \quad (3.2b)$$

with the average droplet and wave energies both taking a form analogous to that of their steady counterparts given in (3.1).

The third canonical regime corresponds to dynamical states that modulate slowly in time. In particular, equation (3.1) approximates quasi-steady dynamics, for which the time scale over which the pilot-wave system evolves greatly exceeds the memory time, and thus one may neglect \dot{E}_p and \dot{E} in (2.5) and (2.17). This slow variation is typical of the low-memory regime and near-critical non-oscillatory perturbations about a steady state, such as the ‘jump up’ and ‘jump down’ instabilities observed in a rotating frame, wherein the droplet shifts to an orbit with larger or smaller orbital radius, respectively (Oza *et al.* 2014b). Similarly, equation (3.2) approximates dynamics consisting of a fast oscillation augmented by slow drift and amplitude modulations. Specifically, the slow drift and amplitude modulations render the average droplet and wave energies over one fast cycle relatively small and thus one may neglect $\langle \dot{E}_p \rangle$ and $\langle \dot{E} \rangle$ when averaging (2.5) and (2.17), respectively. This regime characterises near-critical oscillatory perturbations about a steady state, such as the onset of wobbling of circular orbits arising when a droplet is constrained by an external force (Oza *et al.* 2014b).

The final canonical regime characterises statistically steady states, as might arise for chaotic pilot-wave dynamics in the long-path-memory limit, including the intermittent switching between weakly unstable states when the droplet moves in response to a Coriolis or central force (Harris & Bush 2014; Perrard *et al.* 2014b). Of particular note is the prevalence of wake-like statistics in the hydrodynamic pilot-wave system and their connections to quantum mechanics (Bush & Oza 2021). We assume only that the droplet speed, local wave height and wave energy approach statistically steady states, and that E_p and E are bounded. By taking long-time averages of (2.5) and (2.17), we deduce relationships that are algebraically identical to (3.2), but with angled brackets now denoting long-time averages (Rahman & Kutz 2023).

Equations (3.1) and (3.2) have important consequences for energy evolution in the hydrodynamic pilot-wave system. Notably, the droplet gravitational potential and wave energies both decrease when the droplet speed increases, providing a simple heuristic for distinguishing energetically favourable states. In particular, the energy of an unstable bouncer always exceeds that of a droplet moving at a constant speed (Durey & Milewski 2017; Liu *et al.* 2023). Finally, the bound $E > 0$ imposes a droplet speed limit: specifically, (3.1) implies that $v < c$ for all steady states, while (3.2) implies that $\bar{v} < c$ for all periodic states.

We proceed by demonstrating that the droplet must move at its speed limit in order to maintain a finite local wave height in the high-memory limit. We first note that the wave height of a bouncer, $H_B = AT_M/T_F$, increases linearly with memory. It thus follows from (3.1) that the limit $\lim_{T_M \rightarrow \infty} H = H_0$ for steady droplet motion requires that

$$\lim_{T_M \rightarrow \infty} \frac{AT_M}{T_F} \gamma_D(v) = H_0, \quad (3.3)$$

where $v(T_M)$ is the droplet speed and H_0 is the limiting wave height, which is assumed to be finite and positive. As $\gamma_D(c) = 0$ (see (2.4)), this limit can only be satisfied when

$$v \sim c \left(1 - \frac{H_0 T_F}{2AT_M} \right) \quad \text{as} \quad T_M \rightarrow \infty, \quad (3.4)$$

with a similar relationship holding for the average speed, \bar{v} , of periodic states. Consequently, the speed bounds $v < c$ and $\bar{v} < c$ are necessarily achieved for all steady and periodic states that retain a finite local wave height in the vicinity of the Faraday threshold.

Conversely, the wave energy diverges as the Faraday threshold is approached, by virtue of waves being excited across the entire bath. Specifically, we show in [Appendix C](#) that the energy of the bouncer wave field satisfies the scaling $E_B \sim T_M^2 l_d$ in the high-memory limit, reflecting the diverging wave amplitude and spatial decay length, $l_d(\gamma)$, of the bouncer wave field close the Faraday threshold. For steady states with a finite wave amplitude in the high-memory limit, we combine (3.3) with the relationship $E = \gamma_D(v)E_B$ to deduce that

$$E \sim \frac{H_0 T_F}{A T_M} E_B \quad \text{as } T_M \rightarrow \infty, \tag{3.5}$$

and likewise for periodic states. Consequently, the wave energy dominates the droplet’s kinetic and gravitational potential energies at high memory, as is evident in the energy evolution and partitioning to be considered in § 4.

4. Numerical examples

We proceed to exemplify our theoretical developments (§ 3) through a series of numerical examples. Drawing upon prior theoretical and experimental investigations ([Damiano *et al.* 2016](#); [Couchman *et al.* 2019](#)), we define the axisymmetric wave kernel

$$\mathcal{H}(r) = J_0(k_F r) \left[(1 - \mathcal{S}(k_F r)) + \frac{r}{l_d} K_1(r/l_d) \mathcal{S}(k_F r) \right], \tag{4.1}$$

where K_1 is the modified Bessel function of the second kind of order one. The smoothing function, $\mathcal{S}(x) = e^{-x^{-2}}$, ensures regularity of the wave kernel near the origin, with $\mathcal{S}(x) \rightarrow 0$ as $x \rightarrow 0$ and $\mathcal{S}(x) \rightarrow 1$ as $x \rightarrow \infty$ ([Couchman *et al.* 2019](#)). The exponential far-field spatial decay is characterised by the parameter $l_d = \frac{1}{2} \sqrt{T_M/\alpha}$, which increases with proximity of the vibrational forcing to the Faraday threshold, with α defined in [table 1](#) ([Moláček & Bush 2013b](#)). We consider the regime for which stationary bouncing is unstable, namely $\gamma_W < \gamma < \gamma_F$, where the walking threshold is ([Oza *et al.* 2013](#))

$$\gamma_W = \gamma_F \left(1 - \frac{ck_F T_d}{\sqrt{2}} \right), \tag{4.2}$$

with T_d defined in [table 1](#). We first consider steady walking and orbital motion (§ 4.1), before considering the onset of orbital instability in a rotating frame (§ 4.2). We emphasise that the validity of our theoretical developments is not restricted to the choice of wave kernel considered here.

4.1. Steady droplet motion

For steady droplet motion at speed $v > 0$, the relationship $H = H_B \gamma_D(v)$ and (2.1b) determine that the corresponding memory time, T_M , satisfies

$$1 - \frac{v^2}{c^2} = \frac{1}{T_M} \int_0^\infty \mathcal{H}(\delta(t)) e^{-t/T_M} dt, \tag{4.3}$$

where $\delta(t)$ denotes the droplet displacement over time t . For rectilinear walking, $\delta(t) = vt$, and for orbital motion with radius r_0 , $\delta(t) = 2r_0 |\sin(vt/2r_0)|$. Notably, we parameterise

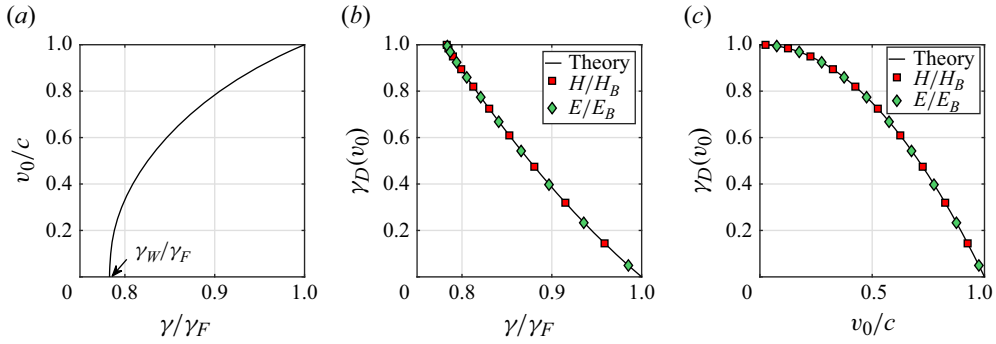


Figure 2. The dependence of energy on the steady rectilinear walking speed, v_0 , computed using (4.3). (a) The free-walking speed increases with the vibrational forcing for $\gamma_W < \gamma < \gamma_F$, approaching the speed limit, c , at the Faraday threshold. (b, c) The magnitude of the local wave height, H (red squares), and stroboscopic wave energy, E (green diamonds), relative to that of a bouncer (H_B and E_B , respectively) as a function of (b) vibrational acceleration, γ , and (c) free-walking speed, v_0 . The numerical results coincide with the theoretical predictions $H/H_B = \gamma_D(v_0)$ and $E/E_B = \gamma_D(v_0)$ for steady droplet motion (see §3) indicated by the black curve, where $\gamma_D(v) = 1 - v^2/c^2$ is the speed-dependent diminution factor (see (2.4)). The physical parameter values are the same as in figure 1.

orbital motion by its radius, as is the case for a droplet moving in response to a Coriolis or central force (Oza *et al.* 2014a; Labousse *et al.* 2016a; Liu *et al.* 2023). We solve (4.3) numerically, and then compute the energy, E (defined in (2.7)), of the accompanying stroboscopic pilot wave using Fourier transforms on a large, doubly periodic domain of size $48\lambda_F \times 48\lambda_F$ with 512×512 grid points. The numerical results are insensitive to increasing the size of the computational domain and to refining the spatial discretisation.

The rectilinear walking speed, v_0 , increases monotonically with the vibrational forcing, approaching the speed limit, c , at the Faraday threshold (see figure 2a). As the droplet walks faster, the local wave height, H , and wave energy, E , both decrease relative to that of a stationary bouncer, denoted H_B and E_B , respectively (see figure 2b,c). The theoretical prediction for the local wave height, $H/H_B = \gamma_D(v_0)$ (see (3.1)), where $\gamma_D(v) = 1 - v^2/c^2$ is the speed-dependent diminution factor, holds exactly for all $\gamma_W < \gamma < \gamma_F$. Despite the theoretical prediction for wave energy, $E/E_B = \gamma_D(v_0)$ (see (3.1)), being formally valid only in the high-memory limit (for which the error in the approximation is of size $O((k_F l_d)^{-1})$), our numerical results demonstrate the efficacy of this prediction both within and beyond the high-memory regime. Indeed, the discrepancy between the theoretical and numerical solutions is visually indistinguishable in figure 2(b,c), with the relative error being less than 1% for all values of γ .

A similar physical picture emerges for orbital states. As the orbital radius, r_0 , is increased, the orbital speed, v , varies with orbital radius, oscillating over half the Faraday wavelength, before approaching the rectilinear walking speed, v_0 , in the large-radius limit (see figure 3a). This speed modulation is a consequence of the increased influence of the droplet’s wake on its motion at high orbital memory (Oza *et al.* 2014a), with similar variations in the local wave height, H , and wave energy, E , evident as the orbital radius is increased (see figure 3b). Despite this more complex dependence on orbital speed, the theoretical predictions prescribed by the speed-dependent diminution factor, γ_D , are in excellent agreement with the numerical results across a wide range of memory and orbital radius. Indeed, the dependences of normalised local wave height, H/H_B , and wave energy, E/E_B , on orbital speed collapse onto the curve $\gamma_D(v)$ for all values of γ

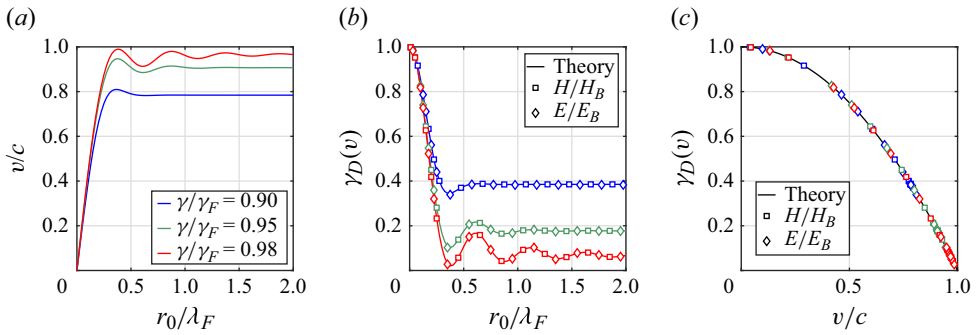


Figure 3. The dependence of energy on the steady orbital speed, v , computed using (4.3) for γ/γ_F taking values 0.9 (blue), 0.95 (green) and 0.98 (red). (a) The orbital speed oscillates over half the Faraday wavelength as the orbital radius, r_0 , is increased, approaching the rectilinear walking speed, v_0 , for large radii. The variations in the orbital speed are most pronounced close to the Faraday threshold. (b, c) The magnitude of the local wave height, H (squares), and stroboscopic wave energy, E (diamonds), relative to that of a bouncer (H_B and E_B , respectively) as a function of (b) orbital radius, r_0 , and (c) orbital speed, v . The numerical results coincide with the theoretical predictions $H/H_B = \gamma_D(v)$ and $E/E_B = \gamma_D(v)$ for steady droplet motion (see § 3) indicated by the black curve, where $\gamma_D(v) = 1 - v^2/c^2$ is the speed-dependent diminution factor (see (2.4)). The physical parameter values are the same as in figure 1.

(see figure 3c), underscoring the universal dependence of energy on speed in orbital pilot-wave dynamics.

Of particular interest is the partitioning of energy in pilot-wave hydrodynamics, which we quantify here for steady walking and orbiting states. To do so, we define the total stroboscopic energy as

$$\mathcal{E} = \frac{1}{2} m |\dot{\mathbf{x}}_p|^2 + mgH + E, \tag{4.4}$$

representing the sum of kinetic, gravitational potential and wave energies. For steady walking and orbiting, we apply the approximations given by (3.1) (as verified in figures 2 and 3) to deduce from (4.4) the approximate relationship

$$\mathcal{E} = \frac{1}{2} m |\dot{\mathbf{x}}_p|^2 + \gamma_D(|\dot{\mathbf{x}}_p|)(mgH_B + E_B), \tag{4.5}$$

which makes clear the dependence on the speed-dependent diminution factor, γ_D , and the relative sizes of the local wave height, H_B , and wave energy, E_B , for stationary bouncing. In particular, we see from (4.5) that the contribution of kinetic energy to the total stroboscopic energy, \mathcal{E} , increases with droplet speed, while the contributions of wave and gravitational potential energies both decrease.

In figure 4, we present the dependence of the total stroboscopic energy on the vibrational forcing for stationary bouncing and steady walking. For both bouncing and walking, the wave energy diverges in the high-memory limit, where the wave field spans the entire plane and so is the main contributor to the total energy (see Appendix C). For steady walking, the kinetic energy increases with the vibrational forcing (consistent with the walking speed curve in figure 2a), while the gravitational potential energy decreases, approaching a finite value in the high-memory limit. The adjustment of the droplet from its wave crest to a region with higher slope is also evident in the wave-field plots in figure 1. Finally, we note that although the gravitational potential energy of a bouncer diverges as the Faraday threshold is approached, this contribution is subdominant to the wave energy, with $mgH_B \ll E_B$ at high memory (see (4.5)).

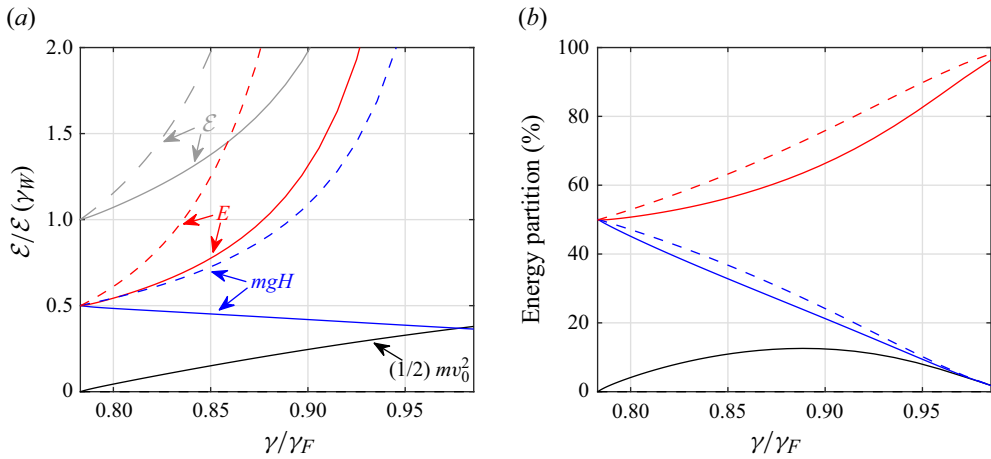


Figure 4. The dependence of the energy partitioning on vibrational forcing for stationary bouncing (dashed curves) and steady walking at the free-walking speed, v_0 (solid curves). (a) The contribution to the total energy, \mathcal{E} (grey, see (4.4)), in terms of the stroboscopic wave energy, E (red), droplet gravitational potential energy, mgH (blue), and droplet kinetic energy, $\frac{1}{2}mv_0^2$ (black). The total energy is normalised by that of a bouncer at the walking threshold, $\mathcal{E}(\gamma_W)$. The wave energy diverges in the high-memory limit for both bouncing and walking. Notably, the droplet gravitational potential energy diverges at high memory for a bouncer, yet decreases towards a finite value (comparable to the kinetic energy) for a walker. (b) The relative contributions of each type of energy to the total energy, with the wave energy dominating in the high-memory limit. The physical parameter values are the same as in figure 1.

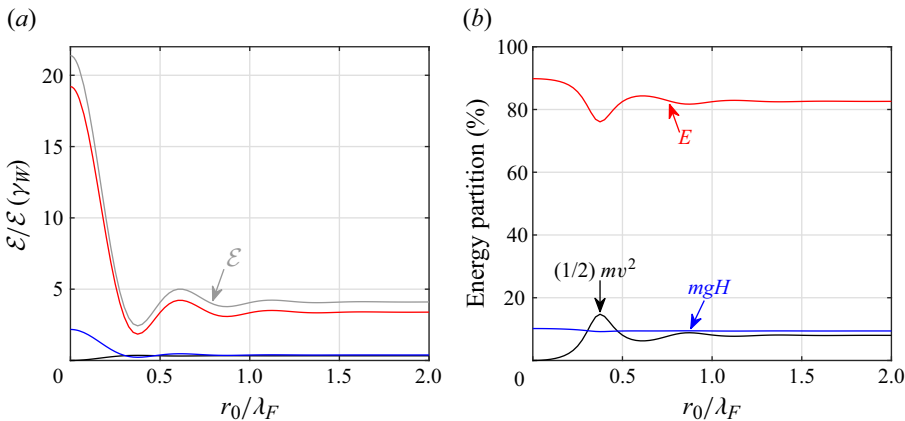


Figure 5. The dependence of the energy partitioning on the orbital radius for steady orbiting at $\gamma/\gamma_F = 0.95$. (a) The contributions to the total energy, \mathcal{E} (grey, see (4.4)), from the stroboscopic wave energy, E (red), droplet gravitational potential energy, mgH (blue), and droplet kinetic energy, $\frac{1}{2}mv^2$ (black). The total energy is normalised by that of a bouncer at the walking threshold, $\mathcal{E}(\gamma_W)$. (b) Energy partition of \mathcal{E} , with minima in the wave and gravitational potential energies corresponding to maxima in the kinetic energy. The physical parameter values are the same as in figure 1.

Similar trends for orbital motion are evident in figure 5. At high memory, the wave energy dominates the droplet kinetic and gravitational potential energies. We note that modulations in the droplet speed with the orbital radius lead to peaks in the partitioning of kinetic energy, and corresponding troughs in the partitioning of wave energy. While it is not easily discernible from figure 5(b), the droplet gravitational potential energy

oscillates in a manner similar to that of the wave energy, by virtue of the relationships $H/H_B = E/E_B = \gamma_D(v)$. As the vibrational forcing is progressively increased, the peaks and troughs in [figure 5\(b\)](#) become more pronounced, and the wave energy dominates the total energy.

4.2. Onset of unstable orbital motion

To investigate the efficacy of (3.2) for slowly varying and periodic states, we consider the onset of orbital instability in a rotating frame. A droplet walking in a rotating frame moves in response to a Coriolis force, $\mathbf{F} = -2m\boldsymbol{\Omega} \times \dot{\mathbf{x}}_p$, where the rotation vector, $\boldsymbol{\Omega} = \Omega \mathbf{e}_z$, is orientated vertically, perpendicular to the droplet's plane of motion (Fort *et al.* 2010; Harris & Bush 2014; Oza *et al.* 2014a). For a droplet moving at steady speed $v = r_0\omega$ along a circular orbit of radius r_0 , we deduce from pilot-wave system (2.1) the radial and tangential force balances:

$$-mr_0\omega^2 = -\frac{mgA}{T_F} \int_0^\infty \mathcal{H}' \left(2r_0 \sin \left(\frac{\omega t}{2} \right) \right) \sin \left(\frac{\omega t}{2} \right) e^{-t/T_M} dt + 2m\Omega r_0\omega, \quad (4.6a)$$

$$Dr_0\omega = -\frac{mgA}{T_F} \int_0^\infty \mathcal{H}' \left(2r_0 \sin \left(\frac{\omega t}{2} \right) \right) \cos \left(\frac{\omega t}{2} \right) e^{-t/T_M} dt, \quad (4.6b)$$

where $\mathcal{H}'(r)$ denotes the derivative of \mathcal{H} with respect to r (with an odd extension so as to be defined over the real line). Notably, one may apply integration by parts to the tangential force balance (4.6b) to deduce the equation for local wave height (4.3) (Oza *et al.* 2014a; Liu *et al.* 2023). Following Oza *et al.* (2014a), we parameterise the circular orbits by their orbital radius for a fixed vibrational forcing: specifically, we fix r_0 and use (4.6b) (or (4.3)) to solve for the orbital frequency, ω , and then use (4.6a) to determine the corresponding bath rotation rate.

We investigate the evolution of the local wave height, $H(t)$, and stroboscopic wave energy, $E(t)$, for an oscillatory instability whose corresponding perturbation grows towards a 2-wobble (Harris & Bush 2014; Oza *et al.* 2014b). We thus anticipate that (3.2) (with $V = 0$) will hold sufficiently close to the instability threshold, for which the instability time scale greatly exceeds the orbital time scale. This behaviour is evidenced in [figure 6](#), for which the local wave height and wave energy when averaged over one speed cycle (denoted $\langle H \rangle/H_B$ and $\langle E \rangle/E_B$, respectively) agree closely with the theoretical predictions made by (3.2) during both the unstable transient and the periodic 2-wobble. Notably, the theoretical prediction for $\langle E \rangle/E_B$ slightly exceeds the accompanying numerical result; this discrepancy is a direct consequence of the high-memory approximation made when deriving (2.17), and so will be less significant closer to the Faraday threshold.

We further test the efficacy of our theoretical predictions by comparing in [figure 7](#) the evolution of dE/dt in the simulations with the theoretical prediction prescribed by (2.17). This investigation is based on the same simulation as in [figure 6](#), but with the focus shifted onto the instantaneous wave energy, rather than that time-averaged over each speed cycle. For the numerical simulations, dE/dt is computed using a second-order finite-difference approximation of $E(t)$, as defined by (2.7). For the theoretical prediction, the numerically computed values of $E(t)$ and $H(t)$ are substituted into the right-hand side of (2.17). Akin to [figure 6\(d\)](#), the theoretical prediction for dE/dt is typically slightly larger than its numerical counterpart, as is most apparent in the unstable transient (see [figure 7a](#)). Nevertheless, there is excellent agreement when the droplet executes the periodic 2-wobble, as demonstrated in [figure 7\(b\)](#) for the final two orbital periods. Our findings verify that (2.17)

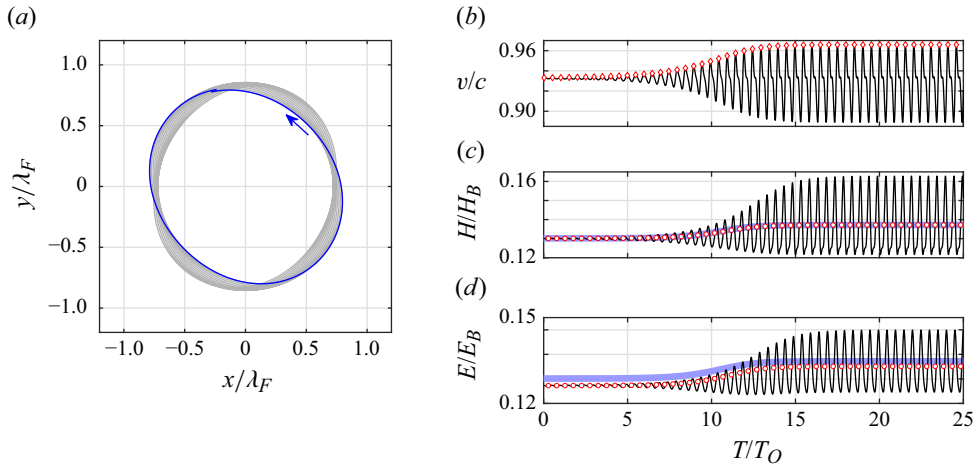


Figure 6. Wobbling motion of an inertial orbit in a frame rotating at $\Omega = -2.78 \text{ rad s}^{-1}$ and vibrating with $\gamma/\gamma_F = 0.96$. (a) Droplet trajectory following a small perturbation from an anticlockwise circular orbit of radius $r_0/\lambda_F = 0.8$. After an initial transient, the trajectory approaches a 2-wobble (grey curve, with the final orbital period denoted in blue). (b) Evolution of the droplet speed (black curve). The red diamonds denote the maxima of each speed cycle, over which the average speed, $\bar{v} = \langle |\dot{x}_p|^2 \rangle^{1/2}$, is computed (see § 3). (c, d) The black curves denote the evolution of (c) the local wave height, H/H_B , and (d) the wave energy, E/E_B , each normalised by that of a stationary bouncer at the same memory. Time is scaled by the orbital period, $T_O = 2\pi/\omega$, of the initial circular orbit. The red circles denote the average values of H/H_B and E/E_B over each speed cycle, and the blue curve denotes the corresponding theoretical prediction given by $\langle H \rangle/H_B = \langle E \rangle/E_B = \gamma_D(\bar{v})$ (see (3.2)). The physical parameter values are the same as in figure 1.

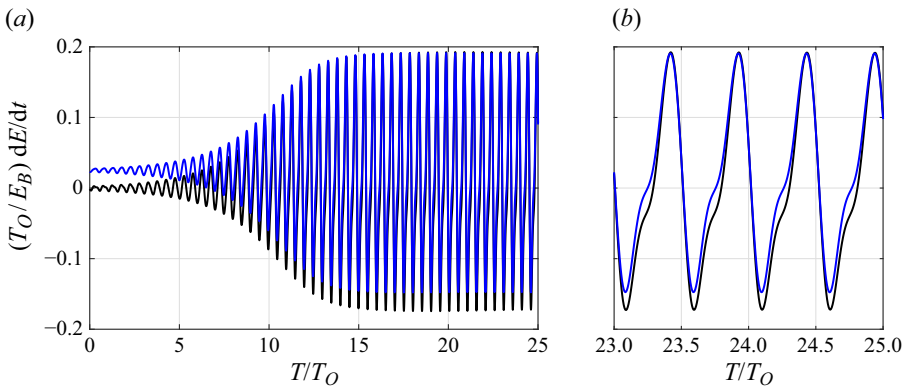


Figure 7. The rate of change of wave energy for a droplet executing the same wobbling trajectory as in figure 6. (a) The black curve denotes dE/dt computed from the simulation, and the blue curve denotes dE/dt as computed from the theoretical prediction (2.17). Time is scaled by the orbital period, T_O , of the initial unstable orbit, and wave energy is normalised by that of a stationary bouncer, E_B , at the same memory. (b) Zoom-in of (a) underscores the efficacy of the theoretical prediction when the droplet executes a 2-wobble.

may be reliably used to investigate the evolution of energy in pilot-wave hydrodynamics, forming a platform on which to base future investigations of unsteady systems.

5. Discussion

Our study has yielded several new insights into the energetics of pilot-wave hydrodynamics. The walking droplet system is damped and driven, with energy input

from the bath vibration and energy dissipated through the action of viscosity. We have paid particular attention to the cases in which these energy inputs and outputs balance, specifically steady and periodic dynamical states, slowly varying states and statistically steady states. For such states, our study illustrates how the partitioning of energy between droplet kinetic energy, droplet gravitational energy and wave energy depends on the system memory. It further illustrates how this partitioning evolves with time for unsteady states. Specifically, the rate of change of droplet energy (2.5) is prescribed by the local wave amplitude relative to that of a bouncer and the diminution factor, $\gamma_D(|\dot{\mathbf{x}}_p|)$, which decreases with the droplet's speed. The rate of change of wave energy (2.17) also depends on the instantaneous wave energy relative to that of a bouncer, and thus the diminution factor, γ_D . Notably, the walker's wave-induced added mass, $m\gamma_B(|\dot{\mathbf{x}}_p|)$, also decreases with its speed (Bush *et al.* 2014). A comparison between γ_B and the energy diminution factor, γ_D , is presented in Appendix D.

Our theoretical developments may be extended in a straightforward fashion in order to treat the energetics of N interacting droplets with constant impact phase, as outlined in Appendix E. In particular, insight into multiple-droplet systems (e.g. lattices or rings) may be gained through consideration of the wave energy, $E(t)$, which evolves according to (E7). For quasi-steady droplet motion, the correspondence

$$\frac{E(t)}{E_B} = \frac{N\bar{H}(t)}{H_B} \tag{5.1}$$

holds, where \bar{H} is the average height of the wave field beneath the droplets, which incorporates wave-mediated inter-droplet spatio-temporal correlations (see (E8)). Consequently, the evolution of the mean lattice wave height may be used as a proxy for that of wave energy for slowly evolving lattices. The decrease in average droplet height between discrete rearrangements of unstable ring structures noted by Couchman & Bush (2020) was thus accompanied by a decrease in the energy of the global pilot-wave field, and so reflects the tendency of multiple-droplet systems to minimise their total energy. We note, however, that (5.1) does not account for dynamic or spatial variations in the droplets' impact phase, and so is not necessarily applicable to irregular or unsteady lattice structures.

It is worth emphasising the generality of our results, but also noting their limitations. In our theoretical developments, we have assumed only that the axisymmetric wave kernel oscillates over the Faraday wavelength and decays exponentially at infinity, with the spatial decay length increasing with proximity to the Faraday threshold. Our results thus apply not only to the particular wave kernel considered in our numerical examples (§4) but to any such pilot-wave form. As a caveat, we note that our results have been deduced from the stroboscopic model, which is based on the assumption of resonance between the droplet and its guiding wave. The role of impact phase is somewhat obscured in the stroboscopic formulation, but becomes clear when one recalls that all of our energetic formulations have been made in terms of the stroboscopic wave height, $h(\mathbf{x}, t)$, rather than the temporally oscillating wave field, $\eta(\mathbf{x}, t) = h(\mathbf{x}, t) \cos(\pi ft)/\mathcal{C}$. Notably, the energy of the stroboscopic wave field, E , is related to the energy of the temporally oscillating wave field averaged over one Faraday period, $\bar{\mathcal{E}}$, via $\bar{\mathcal{E}} = (1/2)E/\mathcal{C}^2$, so the two energies are proportional. As the memory is increased, the phase of drop impact relative to the wave oscillation, \mathcal{C} , also changes, and with it the relative magnitudes of the wave and droplet energies. This dependence is not captured with the stroboscopic model, which assumes that the impact phase is independent of memory. Nevertheless, our results may be applied given the value of \mathcal{C} at a particular memory, as may be measured experimentally.

While the stroboscopic model has been successful in rationalising a number of phenomena in pilot-wave hydrodynamics, it is known to have shortcomings in situations where the droplet's impact phase varies owing to its interaction with a time-varying wave field, as may arise at high memory (Wind-Willassen *et al.* 2013) and in closed settings (Harris *et al.* 2013; Durey *et al.* 2020; Abraham *et al.* 2024). Relaxation of the stroboscopic approximation requires consideration of the droplet's vertical dynamics (Moláček & Bush 2013*a*; Couchman *et al.* 2019; Primkulov *et al.* 2025). Consideration of the energetics in this more general setting will yield insight into the myriad complex periodic, aperiodic and chaotic walking states arising at high memory (Moláček & Bush 2013*b*; Wind-Willassen *et al.* 2013) and will be the subject of future work.

Acknowledgements. The authors thank N. Liu for valuable discussions and D. M. Harris for the photo used in our graphical abstract.

Funding. J.W.M.B. gratefully acknowledges the generous financial support of the NSF through grant CMMI-2154151, and the Office of Naval Research through grant N000014-24-1-2232.

Declaration of interests. The authors report no conflict of interest.

Data availability statement. Data sharing not applicable – no new data generated.

Appendix A. Energy budget

In contrast to the majority of studies on the spontaneous formation of waves above the Faraday threshold (Kumar & Tuckerman 1994; Kumar 1996), the Faraday waves in the walking-droplet system are subcritical, yet sustained by repeated impacts of the droplet on the bath. The energy budget is complex: the energy injection depends on the interference of the waves generated by the moving droplet, and the bath vibration serves to increase the longevity of the waves generated at each impact. These two sources of energy injection may be distinguished by recasting the droplet (2.5) and wave (2.17) energy evolution equations as

$$\frac{dE_p}{dt} + D|\dot{\mathbf{x}}_p|^2 + \frac{mgH(t)}{T_d} = \frac{mgA}{T_F} + \left(\frac{1}{T_d} - \frac{1}{T_M}\right)mgH(t), \quad (\text{A1a})$$

$$\frac{1}{2} \frac{dE}{dt} + \frac{E(t)}{T_d} = \frac{E_B H(t)}{T_M H_B} + \left(\frac{1}{T_d} - \frac{1}{T_M}\right)E(t). \quad (\text{A1b})$$

In both energy equations, the terms on the right-hand side correspond to energy injection through wave creation and bath vibration, respectively. The left-hand side thus describes the energy dissipation, as governed by work done on the droplet by drag (in (A1a) only) and dissipation of the wave field over T_d , the viscous decay time in the absence of vibration.

We proceed to more closely examine the energy injection in (A1). We first note that the energy injection from the bath vibration may be characterised in terms of the effective growth rate

$$\frac{1}{T_d} - \frac{1}{T_M} = \frac{\gamma/\gamma_F}{T_d}, \quad (\text{A2})$$

which describes the decrease in the wave decay rate resulting from bath vibration (Benjamin & Ursell 1954). The energy injection via wave creation is more subtle. The droplet energy injection rate, mgA/T_F in (A1a), is constant, a consequence of the waves generated along the droplet's path being of equal amplitude. In contrast, the wave energy injection rate, $E_B H(t)/T_M H_B$ in (A1b), depends on the local wave height, $H(t)$, which

can vary substantially as the droplet navigates its pilot wave. As the droplet’s dynamics and the constants A , T_M , H_B and E_B appearing in (A1) depend on the proximity of the vibrational acceleration, γ , to the Faraday threshold, γ_F , we conclude that γ/γ_F is the primary factor controlling both forms of energy injection. A more detailed investigation of the system’s energy budget will be the subject of future work.

Appendix B. Energy evolution for the $J_0(k_F r)$ wave kernel

For the dynamics of a single droplet, the exponential spatial decay of the wave field is relatively unimportant (Bush 2015; Bush & Oza 2021), with investigators thus considering the algebraically tractable wave kernel $\mathcal{H}(r) = J_0(k_F r)$ (Oza *et al.* 2013). In this case, the notion of wave energy is somewhat nebulous, with the defining integrals (2.7) of the wave field over the plane being divergent. To circumnavigate this issue, Labousse *et al.* (2016b) and Hubert *et al.* (2022) defined a corresponding wave intensity, denoted $I(t)$, that retained the key features of wave energy whilst being non-divergent. When accounting for the influence of gravitational potential and surface energies for a linear stroboscopic wave field, the wave intensity is defined as (Liu *et al.* 2023)

$$I(t) = \lim_{R_0 \rightarrow \infty} \frac{1}{2R_0} \left[\iint_{|x| < R_0} (\rho g h^2(\mathbf{x}, t) + \sigma |\nabla h|^2) d\mathbf{x} \right], \tag{B1}$$

with $h(\mathbf{x}, t)$ defined by (2.1b) for $\mathcal{H}(r) = J_0(k_F r)$. Notably, the wave intensity defined in (B1) has units of energy per unit length. Owing to the monochromatic form of the pilot wave, one may equivalently express the wave intensity as (Liu *et al.* 2023)

$$I(t) = (\rho g + \sigma k_F^2) \lim_{R_0 \rightarrow \infty} \frac{1}{2R_0} \left[\iint_{|x| < R_0} h^2(\mathbf{x}, t) d\mathbf{x} \right], \tag{B2}$$

which forms the basis for our analysis.

Wave intensity defined in this limiting sense may be better understood by projecting the monochromatic wave field onto the orthogonal eigenfunctions $\Phi_n(\mathbf{x}, k_F) = J_n(k_F r)e^{in\theta}$, in a manner similar to § 2.3. Specifically, by expressing

$$h(\mathbf{x}, t) = \sum_{n=-\infty}^{\infty} a_n(t) \Phi_n(\mathbf{x}, k_F), \text{ where } a_n(t) = \frac{H_B}{T_M} \int_{-\infty}^t \Phi_n^*(\mathbf{x}_p(s), k_F) e^{-(t-s)/T_M} ds \tag{B3}$$

and $H_B = AT_M/T_F$ is the amplitude of the bouncer wave field, it follows from an application of Parseval’s theorem that (Labousse *et al.* 2016b; Hubert *et al.* 2022; Liu *et al.* 2023)

$$I(t) = I_B \sum_{n=-\infty}^{\infty} \frac{|a_n(t)|^2}{H_B^2}, \tag{B4}$$

where

$$I_B = (\rho g + \sigma k_F^2) \lim_{R_0 \rightarrow \infty} \frac{1}{2R_0} \left[\iint_{|x| < R_0} [H_B J_0(k_F |x|)]^2 d\mathbf{x} \right] = (\rho g + \sigma k_F^2) \frac{H_B^2}{k_F} \tag{B5}$$

is the wave intensity of a bouncer.

Notably, (B4) has the same algebraic form as (2.13c), but without the $O((k_F^2 l_d)^{-1})$ correction valid in the high-memory limit; indeed, no approximations have been made when deriving (B4) from (B1). We may thus exploit this correspondence to perform

a series of algebraic steps identical to those presented in § 2.3 to derive, without approximation, the evolution of wave intensity:

$$\frac{dI}{dt} = \frac{2I_B}{T_M} \left(\frac{H(t)}{H_B} - \frac{I(t)}{I_B} \right), \tag{B6}$$

where $H(t) = h(x_p, t)$ is the local wave height. Notably, (B6) is the analogue of the wave energy evolution equation (2.17), thereby demonstrating the generality of the evolution of energy-like wave quantities in terms of the local wave height, $H(t)$. Furthermore, one recovers the relationship $I/I_B = H/H_B$ for steady motion, as derived by Liu *et al.* (2023) for circular orbits. Following a procedure similar to that of § 4, we verified numerically that the approximations to (B6) for canonical pilot-wave dynamics (see § 3) also hold for the wave intensity defined here when considering the wave kernel $J_0(k_F r)$.

Appendix C. Energy of the bouncer wave field

We proceed to determine asymptotic approximations for the energy of the bouncer wave field, E_B (as defined in (2.14)), valid in the high-memory limit. We first derive an asymptotic approximation for an arbitrary wave kernel (Appendix C.1), before seeking a closed-form approximation for E_B when the wave kernel is that used in § 4 (Appendix C.2).

C.1. Asymptotic approximation

In the high-memory limit, the exponential spatial decay length, l_d , of the wave kernel is assumed to diverge. As such, the spectrum of the bouncer wave field is sharply peaked around the Faraday wavenumber, k_F . By taking a Laplace-type approximation of (2.14) for the term related to surface energy, we deduce the high-memory approximation (Borghesi *et al.* 2014)

$$E_B = \pi(\rho g + \sigma k_F^2) \int_0^\infty k \hat{h}_B^2(k) dk. \tag{C1}$$

By applying the Plancherel theorem and using that the bouncer wave field, $h_B(r)$, is related to the wave kernel, $\mathcal{H}(r)$, via $h_B(r) = H_B \mathcal{H}(r)$, we deduce that

$$E_B = \pi(\rho g + \sigma k_F^2) H_B^2 \int_0^\infty r \mathcal{H}^2(r) dr. \tag{C2}$$

Notably, $H_B = AT_M/T_F$ scales linearly with the memory time, T_M , and so diverges in the high-memory limit. Furthermore, as the exponential spatial decay length, l_d , of the wave kernel diverges in the high-memory limit, we posit the scaling $\int_0^\infty r \mathcal{H}^2(r) dr \sim l_d$ as $T_M \rightarrow \infty$. We thus deduce the scaling $E_B \sim l_d T_M^2$ in the high-memory limit, where the precise dependence of l_d on T_M depends on the specific choice of wave kernel.

C.2. Wave kernel used for numerical examples

We proceed by determining an approximate expression for E_B in the high-memory limit for the wave kernel used in § 4, as defined in (4.1). As the function $\mathcal{S}(k_F r)$ primarily controls the smoothness of the wave kernel near the origin and the dominant contribution of the energy at high memory comes from the slow far-field decay, we set $\mathcal{S} = 1$ in (4.1) for the calculation of the wave energy. Consequently, we consider from (C2) the integral

$$\int_0^\infty r \mathcal{H}^2(r) dr = \int_0^\infty r \left[\frac{r}{l_d} K_1(r/l_d) J_0(k_F r) \right]^2 dr, \tag{C3}$$

where the integral may be evaluated using Mathematica to give

$$\int_0^\infty r \mathcal{H}^2(r) dr = \frac{1}{16k_F^2} \left[3 - \frac{4}{(1 + k_F^2 l_d^2)^2} + \left(\frac{1}{k_F l_d} + 3k_F l_d \right) \arctan(k_F l_d) \right]. \quad (C4)$$

We note that

$$\int_0^\infty r \mathcal{H}^2(r) dr \sim \frac{3\pi l_d}{32k_F} \quad \text{for } k_F l_d \gg 1, \quad (C5)$$

consistent with the asymptotic scaling posited in [Appendix C.1](#). We thus conclude from (C2) that the energy of the bouncer wave field for the wave kernel used in § 4 has leading-order behaviour:

$$E_B \sim \frac{3\pi^2}{32} (\rho g + \sigma k_F^2) \frac{A^2 T_M^2 l_d}{T_F^2 k_F} \quad \text{as } T_M \rightarrow \infty, \quad (C6)$$

where $l_d = (1/2)\sqrt{T_M/\alpha}$.

Appendix D. Comparison with the hydrodynamic boost factor

Our investigation into pilot-wave energetics has demonstrated that both the wave energy and droplet gravitational potential energy depend on the droplet’s speed, v , specifically the diminution factor, $\gamma_D(v)$. It is valuable to note that the droplet’s speed also determines its wave-induced added mass; in particular, a droplet executing a slowly accelerating trajectory would appear to have mass $m\gamma_B(v)$ when viewed with no knowledge of the wave field, where $\gamma_B(v) > 1$ is the ‘hydrodynamic boost factor’ (Bush *et al.* 2014). When the distance, vT_M , travelled by the droplet over one memory time is short relative to the spatial decay length, l_d , the droplet’s trajectory may be adequately described by replacing the wave kernel, $\mathcal{H}(r)$, by $J_0(k_F r)$ in (2.1b) (Oza *et al.* 2013; Couchman *et al.* 2019). In this case, the hydrodynamic boost factor is defined as (Bush *et al.* 2014)

$$\gamma_B(v) = 1 + \frac{g A k_F^2 T_M^3}{2T_F (1 + (k_F T_M v)^2)^{3/2}}. \quad (D1a)$$

Evaluating the integral in (4.3) reveals that the diminution factor evaluated at the free-walking speed, $v_0(T_M)$, may be expressed as

$$\gamma_D(v_0) = \frac{1}{(1 + (k_F T_M v_0)^2)^{1/2}}. \quad (D1b)$$

We note in [figure 8](#) that $\gamma_B(v_0)$ decreases with the free-walking speed, $v_0(T_M)$, with a parabolic-like profile similar to that of $\gamma_D(v_0) = 1 - v_0^2/c^2$. This qualitative comparison can be made more explicit by eliminating T_M from (D1), yielding

$$\gamma_B(v_0) = 1 + \frac{g A}{2T_F k_F c^3} (1 + \gamma_D(v_0))^3. \quad (D2)$$

The hydrodynamic boost factor, $\gamma_B(v_0)$, thus also depends on the ratio of the droplet’s free-walking speed, v_0 , to its speed limit, c , and so may be defined in terms of the energy diminution factor, $\gamma_D(v_0) = 1 - v_0^2/c^2$. A deeper discussion of this correlation between $\gamma_B(v_0)$ and $\gamma_D(v_0)$ will appear elsewhere.

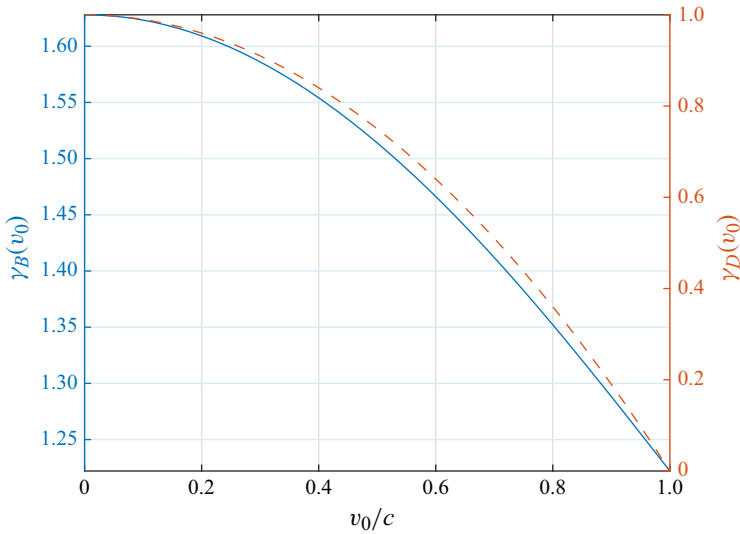


Figure 8. Comparison of the hydrodynamic boost factor, $\gamma_B(v_0)$ (left axis, solid blue curve), and the energy diminution factor, $\gamma_D(v_0)$ (right axis, dashed red curve), evaluated at the free-walking speed, $v_0(T_M)$, for the wave kernel $\mathcal{H}(r) = J_0(k_F r)$. Both $\gamma_B(v_0)$ and $\gamma_D(v_0)$ decrease as the walking speed increases, with the relationship between the two defined in (D2). The physical parameter values are the same as in figure 1.

Appendix E. Energy evolution for interacting droplets

We proceed by considering the energetics of N identical interacting droplets, each with position $\mathbf{x}_i(t)$ (for $i = 1, \dots, N$). We assume that the droplets bounce in resonance with the Faraday wave field, which is subharmonic relative to the bath vibration. Thus, droplet impacts occur in one of two successive cycles of the bath vibration, and droplet pairs may be either in phase or out of phase relative to each other. We thus introduce the parameters $\sigma_i = \pm 1$ to denote the relative bouncing phase of each droplet, with $\sigma_i \sigma_j = 1$ for two droplets bouncing in phase and $\sigma_i \sigma_j = -1$ for out-of-phase bouncing (Couchman *et al.* 2019). The stroboscopic approximation rests on the assumption that temporal variations in the impact phase of each droplet (and thus the wave amplitude, A) are negligible, in which case the stroboscopic model (2.1) takes the form (Couchman *et al.* 2019)

$$m\ddot{\mathbf{x}}_i + D\dot{\mathbf{x}}_i = -mg\sigma_i\nabla h(\mathbf{x}_i, t) + \mathbf{F}_i \quad \text{for } i = 1, \dots, N, \tag{E1a}$$

$$h(\mathbf{x}, t) = \frac{A}{T_F} \sum_{j=1}^N \sigma_j \int_{-\infty}^t \mathcal{H}(|\mathbf{x} - \mathbf{x}_j(s)|) e^{-(t-s)/T_M} ds. \tag{E1b}$$

By modifying the framework developed in § 2, we now establish evolution equations for the droplet and wave energies.

Following an approach similar to that detailed in § 2.2, we define the local wave height beneath each droplet as $H_i(t) = \sigma_i h(\mathbf{x}_i, t)$, where the factor of σ_i accounts for the different wave heights encountered during the different bouncing phases. By performing a calculation similar to that followed for a single droplet, we deduce that

$$\frac{d}{dt} \left(\frac{1}{2} m |\dot{\mathbf{x}}_i|^2 + mg H_i \right) = \dot{\mathbf{x}}_i \cdot \mathbf{F}_i + \frac{mgA}{T_F} \left(\sum_{j=1}^N \sigma_i \sigma_j \mathcal{H}(|\mathbf{x}_i - \mathbf{x}_j|) - \frac{|\dot{\mathbf{x}}_i|^2}{c^2} - \frac{H_i}{H_B} \right) \quad (\text{E2})$$

for $i = 1, \dots, N$, which represents the multiple-droplet extension of (2.3). Notably, the sum in (E2) may be decomposed into the terms for which $j = i$ and $j \neq i$, from which the speed-dependent diminution factor, γ_D , appears naturally within our framework. In the case when the droplets respond to an external potential, $\mathbf{F}_i = -\nabla V(\mathbf{x}_i)$, the energy of each droplet, defined by

$$E_i = \frac{1}{2} m |\dot{\mathbf{x}}_i|^2 + mg H_i + V(\mathbf{x}_i), \quad (\text{E3})$$

evolves according to

$$\frac{dE_i}{dt} = \frac{mgA}{T_F} \left(\gamma_D(|\dot{\mathbf{x}}_i|) - \frac{H_i}{H_B} + \sum_{j \neq i} \sigma_i \sigma_j \mathcal{H}(|\mathbf{x}_i - \mathbf{x}_j|) \right) \quad \text{for } i = 1, \dots, N. \quad (\text{E4})$$

The final term of the right-hand side of (E4) accounts for the change in energy induced by wave-mediated interactions with other droplets. When the droplets are sufficiently distant (specifically, when $|\mathbf{x}_i - \mathbf{x}_j| \gg l_d$ for all $i \neq j$, where l_d is the exponential spatial decay length of the wave kernel), this interaction term may be neglected, in which case (E4) reduces to the energy evolution equation for a single droplet, as prescribed by (2.5).

Following the framework developed in § 2.3, we now determine an evolution equation for the wave energy, E (defined in (2.7)), valid in the high-memory limit. By decomposing the wave field into the orthogonal basis functions $\Phi_n(\mathbf{x}, k)$ with wave mode amplitudes

$$\hat{h}_n(k, t) = \frac{\hat{h}_B(k)}{T_M} \sum_{j=1}^N \sigma_j \int_{-\infty}^t \Phi_n^*(\mathbf{x}_j(s), k) e^{-(t-s)/T_M} ds, \quad (\text{E5})$$

we find that (2.11) and (2.13c) still hold for the case of multiple droplets, while (2.13a) becomes

$$H_i(t) = \sigma_i H_B \sum_{n=-\infty}^{\infty} \frac{\hat{h}_n(k_F, t)}{\hat{h}_B(k_F)} \Phi_n(\mathbf{x}_i(t), k_F) + O((k_F l_d)^{-1}). \quad (\text{E6})$$

Finally, by differentiating (2.13c) with respect to time and using (E5) and (E6), we deduce the leading-order wave energy evolution equation:

$$\frac{dE}{dt} = \frac{2E_B}{T_M} \left(\sum_{j=1}^N \frac{H_j(t)}{H_B} - \frac{E(t)}{E_B} \right), \quad (\text{E7})$$

which is the multiple-droplet analogue of (2.17), valid in the high-memory limit.

For steady and slowly varying configurations, such as lattices (Eddi *et al.* 2009; Couchman *et al.* 2022), rings (Couchman & Bush 2020; Thomson *et al.* 2020a) or orbiting pairs (Protière *et al.* 2006; Oza *et al.* 2017), we deduce from (E4) that the local wave height satisfies

$$H_i = H_B \left(\gamma_D(|\dot{\mathbf{x}}_i|) + \sum_{j \neq i} \sigma_i \sigma_j \mathcal{H}(|\mathbf{x}_i - \mathbf{x}_j|) \right), \quad (\text{E8})$$

and so depends on both the droplet speed (via the diminution factor, γ_D) and the interaction potential, as is mediated by the accompanying Faraday wave field. Furthermore, it follows from (E7) that the wave energy is proportional to the mean wave height beneath the droplets, as expressed in (5.1), which represents the extension of (3.1) to multiple droplets. We thus deduce that the mean gravitational potential energy of droplets in a slowly evolving lattice may be treated as a proxy for wave energy. Finally, similar deductions may be made for periodic and quasi-periodic dynamical states of multiple droplets, including promenading pairs (Borghesi *et al.* 2014; Arbelaziz *et al.* 2018), wobbling orbiting pairs (Oza *et al.* 2017) or various ring oscillations (Couchman & Bush 2020; Thomson *et al.* 2020a, 2021), on the basis of results akin to those derived in § 3.

REFERENCES

- ABRAHAM, A.J., MALKOV, S., LJUBETIC, F.A., DUREY, M. & SÁENZ, P.J. 2024 Anderson localization of walking droplets. *Phys. Rev. X* **14** (3), 031047.
- ABRAMOWITZ, M. & STEGUN, I. 1964 *Handbook of Mathematical Functions*. Dover Publications.
- ARBELAIZ, J., OZA, A.U. & BUSH, J.W.M. 2018 Promenading pairs of walking droplets: dynamics and stability. *Phys. Rev. Fluids* **3** (1), 013604.
- BENJAMIN, T.B. & URSELL, F. 1954 The stability of the plane free surface of a liquid in vertical periodic motion. *Proc. R. Soc. Lond. A: Math. Phys. Sci.* **225** (1163), 505–515.
- BORGHESI, C., MOUKHTAR, J., LABOUSSE, M., EDDI, A., FORT, E. & COUDER, Y. 2014 Interaction of two walkers: wave-mediated energy and force. *Phys. Rev. E* **90** (6), 063017.
- BUSH, J.W.M. 2010 Quantum mechanics writ large. *Proc. Natl Acad. Sci. USA* **107** (41), 17455–17456.
- BUSH, J.W.M. 2015 Pilot-wave hydrodynamics. *Annu. Rev. Fluid Mech.* **47** (1), 269–292.
- BUSH, J.W.M. & OZA, A.U. 2021 Hydrodynamic quantum analogs. *Rep. Prog. Phys.* **84** (1), 017001.
- BUSH, J.W.M., OZA, A.U. & MOLÁČEK, J. 2014 The wave-induced added mass of walking droplets. *J. Fluid Mech.* **755**, R7.
- COUCHMAN, M.M.P. & BUSH, J.W.M. 2020 Free rings of bouncing droplets: stability and dynamics. *J. Fluid Mech.* **903**, A49.
- COUCHMAN, M.M.P., EVANS, D.J. & BUSH, J.W.M. 2022 The stability of a hydrodynamic Bravais lattice. *Symmetry* **14** (8), 1524.
- COUCHMAN, M.M.P., TURTON, S.E. & BUSH, J.W.M. 2019 Bouncing phase variations in pilot-wave hydrodynamics and the stability of droplet pairs. *J. Fluid Mech.* **871**, 212–243.
- COUDER, Y., FORT, E., GAUTIER, C.-H. & BOUDAUD, A. 2005a From bouncing to floating: noncoalescence of drops on a fluid bath. *Phys. Rev. Lett.* **94** (17), 177801.
- COUDER, Y., PROTIÈRE, S., FORT, E. & BOUDAUD, A. 2005b Walking and orbiting droplets. *Nature* **437** (7056), 208–208.
- DAMIANO, A.P., BRUN, P.-T., HARRIS, D.M., GALEANO-RIOS, C.A. & BUSH, J.W.M. 2016 Surface topography measurements of the bouncing droplet experiment. *Exp. Fluids* **57** (163), 1–7.
- DOUADY, S. 1990 Experimental study of the Faraday instability. *J. Fluid Mech.* **221**, 383–409.
- DUREY, M. & MILEWSKI, P.A. 2017 Faraday wave-droplet dynamics: discrete-time analysis. *J. Fluid Mech.* **821**, 296–329.
- DUREY, M., MILEWSKI, P.A. & BUSH, J.W.M. 2018 Dynamics, emergent statistics, and the mean-pilot-wave potential of walking droplets. *Chaos* **28** (9), 096108.
- DUREY, M., MILEWSKI, P.A. & WANG, Z. 2020 Faraday pilot-wave dynamics in a circular corral. *J. Fluid Mech.* **891**, A3.
- EDDI, A., DECELLE, A., FORT, E. & COUDER, Y. 2009 Archimedean lattices in the bound states of wave interacting particles. *Europhys. Lett.* **87** (5), 56002.
- EDDI, A., SULTAN, E., MOUKHTAR, J., FORT, E., ROSSI, M. & COUDER, Y. 2011 Information stored in Faraday waves: the origin of a path memory. *J. Fluid Mech.* **674**, 433–463.
- ELLEGAARD, C. & LEVINSSEN, M.T. 2020 Interaction of wave-driven particles with slit structures. *Phys. Rev. E* **102** (2), 023115.
- FORT, E., EDDI, A., BOUDAUD, A., MOUKHTAR, J. & COUDER, Y. 2010 Path-memory induced quantization of classical orbits. *Proc. Natl Acad. Sci. USA* **107** (41), 17515–17520.
- HARRIS, D.M. & BUSH, J.W.M. 2014 Droplets walking in a rotating frame: from quantized orbits to multimodal statistics. *J. Fluid Mech.* **739**, 444–464.
- HARRIS, D.M., MOUKHTAR, J., FORT, E., COUDER, Y. & BUSH, J.W.M. 2013 Wavelike statistics from pilot-wave dynamics in a circular corral. *Phys. Rev. E* **88** (1), 011001.

- HUBERT, M., PERRARD, S., VANDEWALLE, N. & LABOUSSE, M. 2022 Overload wave-memory induces amnesia of a self-propelled particle. *Nat. Commun.* **13** (1), 4357.
- KUMAR, K. 1996 Linear theory of faraday instability in viscous fluids. *Proc. R. Soc. Lond. A: Math. Phys. Engng Sci.* **452** (1948), 1113–1126.
- KUMAR, K. & TUCKERMAN, L.S. 1994 Parametric instability of the interface between two fluids. *J. Fluid Mech.* **279**, 49–68.
- KUTZ, J.N., RAHMAN, A., EBERS, M.R., KOCH, J. & BRAMBURGER, J.J. 2022 Universal dynamics of damped-driven systems: the logistic map as a normal form for energy balance. <https://arxiv.org/abs/2211.11748>.
- LABOUSSE, M., OZA, A.U., PERRARD, S. & BUSH, J.W.M. 2016a Pilot-wave dynamics in a harmonic potential: quantization and stability of circular orbits. *Phys. Rev. E* **93** (3), 033122.
- LABOUSSE, M., PERRARD, S., COUDER, Y. & FORT, E. 2016b Self-attraction into spinning eigenstates of a mobile wave source by its emission back-reaction. *Phys. Rev. E* **94** (4), 042224.
- LIU, N., DUREY, M. & BUSH, J.W.M. 2023 Pilot-wave dynamics in a rotating frame: the onset of orbital instability. *J. Fluid Mech.* **973**, A4.
- MOLÁČEK, J. & BUSH, J.W.M. 2013a Drops bouncing on a vibrating bath. *J. Fluid Mech.* **727**, 582–611.
- MOLÁČEK, J. & BUSH, J.W.M. 2013b Drops walking on a vibrating bath: towards a hydrodynamic pilot-wave theory. *J. Fluid Mech.* **727**, 612–647.
- OZA, A.U., HARRIS, D.M., ROSALES, R.R. & BUSH, J.W.M. 2014a Pilot-wave dynamics in a rotating frame: on the emergence of orbital quantization. *J. Fluid Mech.* **744**, 404–429.
- OZA, A.U., ROSALES, R.R. & BUSH, J.W.M. 2013 A trajectory equation for walking droplets: hydrodynamic pilot-wave theory. *J. Fluid Mech.* **737**, 552–570.
- OZA, A.U., SIÉFERT, E., HARRIS, D.M., MOLÁČEK, J. & BUSH, J.W.M. 2017 Orbiting pairs of walking droplets: dynamics and stability. *Phys. Rev. Fluids* **2** (5), 053601.
- OZA, A.U., WIND-WILLASSEN, Ø., HARRIS, D.M., ROSALES, R.R. & BUSH, J.W.M. 2014b Pilot-wave hydrodynamics in a rotating frame: exotic orbits. *Phys. Fluids* **26** (8), 082101.
- PERRARD, S., LABOUSSE, M., FORT, E. & COUDER, Y. 2014 A chaos driven by interfering memory. *Phys. Rev. Lett.* **113** (10), 104101.
- PERRARD, S., LABOUSSE, M., MISKIN, M., FORT, E. & COUDER, Y. 2014b Self-organization into quantized eigenstates of a classical wave-driven particle. *Nat. Commun.* **5** (1), 3219.
- PRIMKULOV, B.K., EVANS, D.J., BEEN, J.B. & BUSH, J.W.M. 2025 Non-resonant effects in pilot-wave hydrodynamics. *Phys. Rev. Fluids* **10** (1), 013601.
- PROTIÈRE, S., BOUDAUD, A. & COUDER, Y. 2006 Particle-wave association on a fluid interface. *J. Fluid Mech.* **554** (–1), 85–108.
- RAHMAN, A. & KUTZ, J.N. 2023 Walking droplets as a damped-driven system. *SIAM J. Appl. Dyn. Syst.* **22** (2), 1219–1233.
- TADRIST, L., SHIM, J.-B., GILET, T. & SCHLAGHECK, P. 2018 Faraday instability and subthreshold Faraday waves: surface waves emitted by walkers. *J. Fluid Mech.* **848**, 906–945.
- TAMBASCO, L.D., HARRIS, D.M., OZA, A.U., ROSALES, R.R. & BUSH, J.W.M. 2016 The onset of chaos in orbital pilot-wave dynamics. *Chaos* **26** (10), 103107.
- THOMSON, S.J., COUCHMAN, M.M.P. & BUSH, J.W.M. 2020a Collective vibrations of confined levitating droplets. *Phys. Rev. Fluids* **5** (8), 083601.
- THOMSON, S.J., DUREY, M. & ROSALES, R.R. 2020b Collective vibrations of a hydrodynamic active lattice. *Proc. R. Soc. Lond. A: Math. Phys. Engng Sci.* **476** (2239), 20200155.
- THOMSON, S.J., DUREY, M. & ROSALES, R.R. 2021 Discrete and periodic complex Ginzburg–Landau equation for a hydrodynamic active lattice. *Phys. Rev. E* **103** (6), 062215.
- TURTON, S.E., COUCHMAN, M.M.P. & BUSH, J.W.M. 2018 A review of the theoretical modeling of walking droplets: toward a generalized pilot-wave framework. *Chaos* **28** (9), 096111.
- WIND-WILLASSEN, Ø., MOLÁČEK, J., HARRIS, D.M. & BUSH, J.W.M. 2013 Exotic states of bouncing and walking droplets. *Phys. Fluids* **25** (8), 082002.